Pacific Northwest
NATIONAL LABORATORY

PNNL-38319

# A spline-based method to obtain spatially dependent viscosity in confined flows

September 2025

Jaehun Chun
Bruce J Palmer
Pauline Simonnin

U.S. DEPARTMENT of ENERGY

Prepared for the U.S. Department of Energy
under Contract DE-AC05-76RL01830

## DISCLAIMER



PACIFIC NORTHWEST NATIONAL LABORATORY
*operated by*
BATTELLE
*for the*
UNITED STATES DEPARTMENT OF ENERGY
*under Contract DE-AC05-76RL01830*

**Printed in the United States of America**

**Available to DOE and DOE contractors from**
**the Office of Scientific and Technical Information,**
**P.O. Box 62, Oak Ridge, TN 37831-0062**
**www.osti.gov**
**ph: (865) 576-8401**
**fox: (865) 576-5728**
**email: reports@osti.gov**

**Available to the public from the National Technical Information Service**
**5301 Shawnee Rd., Alexandria, VA 22312**
**ph: (800) 553-NTIS (6847)**
**or (703) 605-6000**
**email: info@ntis.gov**
**Online ordering: http://www.ntis.gov**

PNNL-38319

# A spline-based method to obtain spatially dependent viscosity in confined flows

September 2025

Jaehun Chun
Bruce J Palmer
Pauline Simonnin

Prepared for
the U.S. Department of Energy
under Contract DE-AC05-76RL01830

Pacific Northwest National Laboratory
Richland, Washington 99354

# Abstract

Coupling chemical physics to continuum theories is a critical step to understanding multi-scale phenomena. This paper will connect non-equilibrium molecular dynamics simulations to a continuum-based Navier-Stokes equation that has relaxed the assumption of spatial uniformity in viscosity. Using a form for viscosity based on spline interpolation, viscosity as a function of position is obtained from the least squares fit of the velocity profile measured from molecular simulations of flow in a nanochannel. Viscosity can vary widely, particularly near the channel boundaries, indicating that uniform viscosity is no longer appropriate. Variations of the viscosity near the channel surfaces imply that considering solution and surface chemistry could be necessary to rigorously understand molecular-scale flows in nanochannels.

https://doi.org/10.26434/chemrxiv-2025-qzmx9

# Acknowledgments

This research was supported by the Non-Equilibrium Transport Driven Separations Initiative (NETS), under the Laboratory Directed Research and Development (LDRD) Program at Pacific Northwest National Laboratory (PNNL). PNNL is a multi-program national laboratory operated for the U.S. Department of Energy (DOE) by Battelle Memorial Institute under Contract No. DE-AC05-76RL01830. The authors also wish to thank Greg Schenter and Chris Mundy for many useful discussions.

# 1.0 Introduction

The extraction of macroscopic equilibrium and non-equilibrium transport properties from molecular dynamics simulations is a long-standing problem in statistical mechanics. Equilibrium properties can usually be obtained either through direct averages of appropriate variables or by examining the magnitude of fluctuations [1]. Non-equilibrium transport properties can be obtained either by integrating the auto-correlation function of some variable over time using a Green-Kubo relation [2,3] or by applying a field to the system and directly measuring the response. The latter is the approach used in non-equilibrium molecular dynamics (NEMD) simulations. Simulation of flow in a nanochannel to obtain the shear viscosity was one of the earliest attempts to directly calculate a macroscopic transport property using NEMD. The original paper of Lees and Edwards [4] introduced the concept of sliding periodic boundary conditions that enabled simulations of a flow gradient without introducing physical boundaries to the system. This minimized the introduction of artifacts associated with the boundary and helped reduce the size of the simulations required to obtain accurate results. The $xy$ component of the stress tensor, $\sigma_{xy}$ was calculated from the simulation and used to find the viscosity $\mu$ by taking the ratio of the stress tensor component and the gradient of the velocity

$$\sigma_{xy}/(du_y/dx) = \mu$$

A significant concern with the NEMD approach was that the flow velocity used in the simulations were typically much larger than anything used in the corresponding real-world experiments. The necessity for using such high flow velocities derived from both the need to extract useful information from a simulation representing a short time interval (typically on the order of nanoseconds) and the relatively high velocity of atoms in the simulation due to thermal motion. Molecules at room temperature have velocities on the order of hundreds of meters per second and this provides a very noisy background from which to extract a much slower steady flow. Further, the high flow velocity could also potentially impact the simulations by steadily raising the temperature via viscous heating. However, in spite of the high flow rates, it was found that viscous heating was relatively small over intervals that were sufficient to estimate the viscosity.

Gosling, McDonald and Singer [5] simplified the determination of the viscosity by applying a steady sinusoidal force to the simulation cell that produced a stationary flow that also varied sinusoidally. Comparing the stationary field with the continuum solution for the same configuration allowed the authors to calculate the viscosity. Note that this approach can remove the necessity of evaluating the microscopic stress tensor, which is itself a potentially complicated and time-consuming calculation. This was one of the first attempts to evaluate the viscosity by comparing the flow field of a forced molecular simulation with the solution of a corresponding macroscopic continuum problem.

Later work by Evans and Morris [6] expanded on the NEMD approach by developing equations of motion that created appropriate non-equilibrium fluxes that could be used in conjunction with linear response theory to calculate transport coefficients. These systems no longer correspond to Hamiltonian dynamics but under suitable restrictions still preserve the incompressibility of phase space and hence linear response is still applicable [6.7]. Furthermore, the equations of motion can be modified to not only produce the desired flow in response to an external field but also to correct for additional effects, such as viscous heating, by thermostatting the simulation to maintain a constant temperature.

NEMD calculations originally focused on evaluating zero wavevector properties needed for simulations at macroscopic scales. However, later researchers began investigating flow in nanochannels as interesting in itself and not just as a proxy for flows in larger systems. At the nanoscale, a number of assumptions about flow in a channel (e.g., that an infinitesimal fluid element at the continuum scale is much larger than the length scale associated with individual molecules) break down and deviations from classical behavior are observed [8]. Near the boundaries of the channel, the confined fluid can become significantly structured [9,10] and the assumption that the fluid is uniform in the channel and that properties of the fluid are the same everywhere in the system are not expected to be valid. In addition, interactions between the fluid and the channel surface can create boundary effects that can alter assumptions about flow at the boundary [8] and even assumptions about where the surface is located.

An early effort to look at flow in a microchannel via NEMD was reported by Todd, Evans and Davis [11]. They studied variations in the shear stress and the shear viscosity near the boundaries of the channel for a simple atomic fluid moved by a uniform force field to produce a parabolic Poiseuille-like flow profile. This study calculated the components of the stress tensor directly from a microscopic expression and also computed it by integrating the classical momentum conservation expression. For larger channels integration appeared to work well, but later work by Travis, Todd and Evans [12] suggested that for narrower channels, this approach breaks down.

Another approach to extracting viscosity from molecular simulations of Poiseuille flow was to fit the flow profile to a parabola and use the known classical solution to the problem to back out the viscosity [13,14]. This is straightforward to implement but requires some adjustments if flow near the boundaries deviates from a classic parabolic shape. This paper will generalize this approach by assuming that the viscosity is a function of position in the channel. In this case, the parabolic solution is no longer valid but the viscosity can still be extracted from the simulation by fitting the viscosity function in the Navier-Stokes equation to the flow profiles measured from simulations. This is straightforward, since the only inputs are the velocity and a force profile, both of which are easily measured directly from the simulation. Spline fits are used to allow multiple simulation data to contribute to the determination of each fit parameter and produce a smooth profile for the viscosity but still allow for local variations that reflect changes in local properties inside the fluid.

# 2.0 Methods

The viscosity profiles calculated in this paper are based on the Navier-Stokes equation for incompressible fluid flow, which has the form [15]

$$\rho\frac{\partial\vec{u}}{\partial t}+\rho(\vec{u}\cdot\nabla)\vec{u}=-\nabla p+\rho\bar{g}+\nabla\cdot\bar{\bar{\sigma}} \quad (1)$$

The mass density is $\rho$, the local velocity field $\vec{u}$, the pressure is $p$, the acceleration of gravity is $\bar{g}$ and the stress tensor due to shear is $\bar{\bar{\sigma}}$. This paper is only concerned with laminar, incompressible flow between two parallel surfaces. In this case, the only non-zero component of $\vec{u}$ is $u_y$, assuming that the parallel surfaces are perpendicular to the x-axis and that the applied force on the fluid is parallel to the $y$ axis. Under these conditions, the right-hand side of equation (1) is zero and the shear stress term in equation (1) reduces to

$$\frac{\partial}{\partial x}\mu(x)\frac{\partial}{\partial x}u_y(x) \quad (2)$$

assuming a non-uniform viscosity. For a gravity-driven flow, the governing equation is then

$$\frac{\partial}{\partial x}\mu(x)\frac{\partial}{\partial x}u_y(x)=-\rho g \quad (3)$$

A schematic of the simulation setup based on this geometry is shown in figure (1).

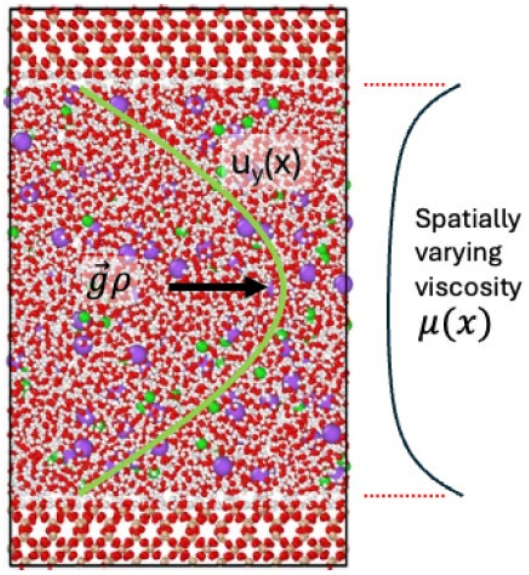


Figure 1. Schematic diagram showing the spline based fitting method coupled with NEMD simulations of parabolic flow in a nanochannel

This paper will focus on developing a methodology for fitting the spatially dependent viscosity parameter $\mu(x)$ in equation (3) using velocity profiles generated from NEMD simulations. The first step in generating a profile is to create a discretized form of the operator acting on $u_y(x)$. The

channel is assumed to have width $L$ and the velocity in the $y$-direction vanishes at the channel boundaries located at $x = 0$ and $x = L$. The interval $[0, L]$ is divided into $N$ increments of size $\Delta x = L/N$. The momentum $\rho u_y$ is a conserved quantity, so it is possible to use a finite-volume approach on equation (3). The momentum $\rho u_y$ satisfies the conservation equation

$$\Delta x \frac{\partial u_{y,i}}{\partial t} = -(\psi_{i+} + \psi_{i-}) \qquad (4)$$

where $i$ is the index of some increment in $[0, L]$ and $\psi_{i\pm}$ is the flux of $u_y$ out of the increment at the high (+) or low (−) end repsectively. From the divergence theorem, the right-hand side of this equation is equivalent to the operator in equation (3).

The $y$ component of momentum is transferred between cells via a diffusive flux that is proportional to the gradient of $u_y$ in the $x$ direction, $j_{u_y} = -\mu\, \partial u_y / \partial x$. For cells that do not have a channel boundary on one side or the other, the gradient of $u_y$ can be approximated using a first order finite difference

$$\psi_{i\pm} = -\frac{\mu_{i\pm1} + \mu_i}{2} \frac{u_{y,i\pm1} - u_{y,i}}{\Delta x} \qquad (5)$$

This equation assumes that all values are defined at cell centers. The value of $\mu$ at the interface between the two cells is the average of the value defined at the centers of the two cells on either side of the interface. For the two cells at the edges of the channel, there is no cell on the other side of the interface so this formula no longer works. The value of $u_y$ at the boundaries is defined to be zero, so the gradient can be approximated on the half-interval of length $\Delta x/2$ between the cell center and the cell edge. The value of the viscosity is assumed to be constant on this interval and equal to the value in the cell center. For cell 1 bordering the edge at $x = 0$, the flux is then

$$\begin{aligned} \psi_{1-} &= -\mu_1 \frac{(u_{y,0} = 0) - u_{y,1}}{\Delta x/2} \\ &= \mu_1 \frac{2u_{y,1}}{\Delta x} \end{aligned} \qquad (6)$$

Similarly, at cell $N$ bordering the edge a $x = L$,

$$\begin{aligned} \psi_{N+} &= -\mu_N \frac{(u_{y,N+1} = 0) - u_{y,N}}{\Delta x/2} \\ &= \mu_N \frac{2u_{y,N}}{\Delta x} \end{aligned} \qquad (7)$$

If $\mu$ is assumed constant throughout the channel, then equation (4) for an interior cell reduces to

$$\frac{\partial u_{y,i}}{\partial t} = \mu \frac{u_{k,i+1} - 2u_{y,i} + u_{y,i-1}}{\Delta x^2} \qquad (8)$$

The right-hand side of the equation is proportional to the standard second order finite difference approximation to a second derivative.

Using the flux expressions in equation (4), a discretized version of equation (3) can be written as

$$\overline{\overline{K}} \cdot \overline{u}_y = g\overline{\rho} \qquad (9)$$

The elements of $\overline{\overline{K}}$ are

$$\begin{aligned} K_{i,i+1} &= \frac{\mu_{i+1}+\mu_i}{2}\frac{u_{y,i+1}-u_{u,i}}{\Delta x^2}(1-\delta_{i,N}) \\ K_{i,i} &= -\frac{\mu_{i+1}+\mu_i}{2}\frac{u_{y,i+1}-u_{u,i}}{\Delta x^2}(1-\delta_{i,N}) \\ &- \frac{\mu_{i-1}+\mu_i}{2}\frac{u_{y,i-1}-u_{u,i}}{\Delta x^2}(1-\delta_{i,1}) \\ &- \mu_N\frac{2u_{y,N}}{\Delta x^2}\delta_{i,N} - \mu_1\frac{2u_{i,1}}{\Delta x^2}\delta_{i,1} \\ K_{i,i-1} &= \frac{\mu_{i-1}+\mu_i}{2}\frac{u_{y,i-1}-u_{u,i}}{\Delta x^2}(1-\delta_{i,1}) \end{aligned}$$

Given the force array $g\bar{\rho}$ due to gravity, the velocity profile $\bar{u}_y$ can be found by inverting $\overline{\overline{K}}$. This can be used to construct an objective function $\chi$ for a least squares regression

$$\chi = \left(\overline{\overline{K}}^{-1} \cdot g\overline{\rho} - \overline{u}_y\right)^2 \qquad (10)$$

A calculation based on this equation was implemented using the PETSc/TAO optimization library [16] and used to obtain a viscosity profile from a velocity profile. The optimizations reported here used the Limited-Memory, Variable-Metric (LMVM) method. This method requires gradients of the objective function, and these can be calculated if the gradients of the inverse of $\overline{\overline{K}}$ are known. These, in turn, are given by

$$\nabla_{\overline{\mu}}\overline{\overline{K}}^{-1} = \overline{\overline{K}}^{-1} \cdot \nabla_{\overline{\mu}}\overline{\overline{K}} \cdot \overline{\overline{K}}^{-1}$$

where $\bar{\mu}$ is a vector that represents the value of $\mu$ at each of the points in the velocity profile. For each value of $\mu_i$, the matrix $\nabla_{\mu_i}\overline{\overline{K}}$ is quite sparse and contains at most 3 nonzero entries. This can be used to speed up calculations of the gradient.

In the simplest case, the fit parameters are the viscosities $\mu_i$ at each cell center, so the number of fit parameters ($\{\mu_i\}$) is equal to the number of measurements ($\{\mu_{y,i}\}$). However, this appears to be very unstable and produces poor results in the center of the channel. As a test, a parabolic profile, corresponding to an analytic solution of equation (3) for a uniform viscosity, was used as the input vector $\bar{u}_y$. The profile is given by

$$u_y(x) = \frac{\rho g}{2\mu}x(L-x) \qquad (11)$$

and values of $\mu$ = 25, $L$ = 100 and $\rho g$ = 1 were used to generate $u_y(x)$ at 200 evenly spaced points on the $x$-axis. Figure (2) compares the original profile generated from equation (11) and the profile reconstituted using equation (9) with a fitted viscosity profile. The original and

reconstituted profiles are close to each other but the fitted viscosity profile, shown in figure 3, deviates noticeably from the expected value of 25 in the center of the channel. In this region, the shear is relatively low and the value of the viscosity may have little effect on the shape of the velocity profile, resulting in large deviations from the expected behavior.

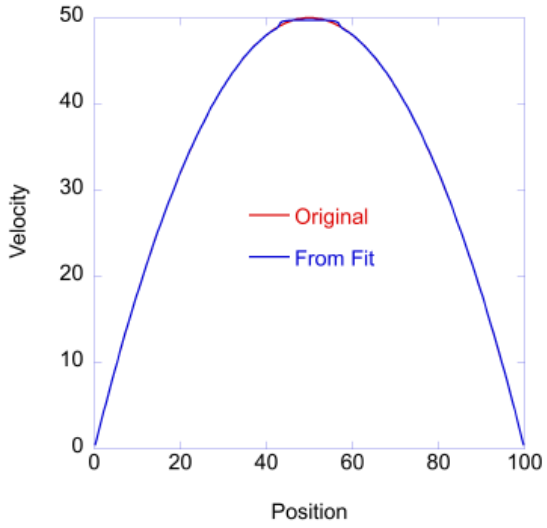


Figure 2. Parabolic velocity profile from equation (11) (red) and profile generated from least squares fit to the parabola (blue).

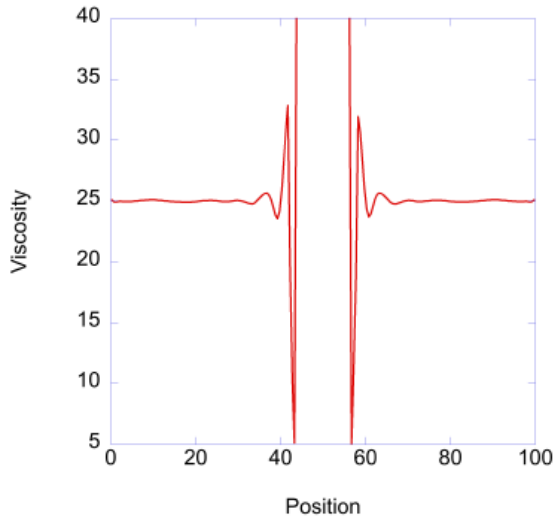


Figure 3. Viscosity profile derived from fit to parabolic velocity profile. Expected curve is a horizontal line with value 25.

A possible remedy for the instability in the center is to reduce the number of variables used to describe the viscosity profile, so that more data points are used to determine each parameter. One way to do this is to represent the viscosity profile using cubic splines [17]. In this approach, the channel width $L$ is divided into $K$ intervals, each of length $L/K$. The endpoints of the intervals are at the locations $\zeta_k$, where $k \in [1, K+1]$. The original measurements are at the locations $x_i$, $i \in [1, N]$ and the endpoints of the spline locations are chosen to coincide with the first and last measurement locations such that $\zeta_1 = x_1$ and $\zeta_{K+1} = x_N$. The locations marking the endpoints of

the spline intervals are referred to in spline terminology as “knots”. In between knots $k$ and $k+1$, the viscosity is described by the cubic polynomial

$$\mu(x) = \sum_{n=0}^{3} a_n^k (x-\zeta_k)^n \qquad x \in [\zeta_k, \zeta_{k+1}] \quad (12)$$

At the knots, the spline function takes on the values $\eta_k$ and these values are the parameters determined by the fit. The coefficients $a_n^k$ are determined by requiring that the spline fit has the values $\eta_k$ at the knots, that it be continuous at the knots and its first and second derivatives be continuous at the knots. The continuity conditions can only be applied to interior knots so an additional condition at the endpoints is that the second derivative is zero. This is a commonly used boundary condition in spline fits and corresponds to a linear profile at the edges of the fitted region. The two conditions at each of the endpoints means that the number of conditions matches the number of unknowns, so the problem is well-posed. A linear profile at the endpoints also matches the behavior seen in viscosity profiles obtained by other means [18]. It is, however, at odds with the approximation made in evaluating the boundary conditions in equations (6) and (7) that assumed that the viscosity profile is flat near the boundaries. However, the increments in the data are typically much smaller than the spacing between knots, so the requirement that the profile is constant near the boundary applies at a much smaller scale than the boundary condition for the splines.

The conditions on the spline fit at the knots lead to the following conditions on the $a_n^k$:

For knot $k = 1$

$$\begin{aligned} a_0^1 &= \eta_1 \\ 2a_2^1 &= 0 \end{aligned}$$

For knots $k \in [2, K]$

$$\begin{aligned} \sum_{n=0}^{3} a_n^{k-1} (\zeta_k - \zeta_{k-1})^n &= \eta_k \\ a_0^k &= \eta_k \\ \sum_{n=1}^{3} a_n^{k-1} n (\zeta_k - \zeta_{k-1})^{n-1} - a_1^k &= 0 \\ \sum_{n=2}^{3} a_n^{k-1} n(n-1)(\zeta_k - \zeta_{k-1})^{n-2} - 2a_2^k &= 0 \end{aligned}$$

For knot $k = K + 1$

$$\begin{aligned} \sum_{n=0}^{3} a_n^K (\zeta_{K+1} - \zeta_K)^n &= \eta_{K+1} \\ \sum_{n=2}^{3} a_n^K n(n-1)(\zeta_{K+1} - \zeta_K)^{n-2} &= 0 \quad (13) \end{aligned}$$

These conditions are sufficient to determine the $a_n^k$ uniquely. Equations (13) are linear in the spline coefficients, so it is possible to write (13) as a matrix equation of the form

$$\overline{\overline{X}} \cdot \bar{a} = \bar{\pi} \qquad (14)$$

where $\overline{\overline{X}}$ is a $4K \times 4K$ matrix and $\bar{a}$ and $\bar{\pi}$ are vectors of length $4K$. The vector $\bar{\pi}$ is zero except at those locations corresponding to the conditions that the spline function equal $\eta_k$ at the values $x = \zeta_k$. Those locations have the values $\eta_k$. Equation (14) can be formally solved to get the coefficients $\bar{a}$

$$\overline{\overline{X}}^{-1} \cdot \bar{\pi} = \bar{a} \qquad (15)$$

The value of the viscosity $\mu$ at any point $x$ is a function of the $a_n^k$, which are, in turn, a function of the spline values $\eta_k$. To fit the velocity profile by optimizing the objective function $\chi$, we need gradients of $\chi$ with respect to the spline values $\bar{\eta}$. The only term that depends directly on the spline values is $\bar{\pi}$, so the gradient of $\bar{a}$ with respect to the $\bar{\eta}$ is

$$\nabla_{\bar{\eta}} \bar{a} = \overline{\overline{X}}^{-1} \cdot \nabla_{\bar{\eta}} \bar{\pi} \qquad (16)$$

Although the original matrix $\overline{\overline{X}}$ is sparse, its inverse is dense so each of the $a_n^k$ will potentially depend on the spline values at all of the knots. Using equation (16), the gradients of the spline coefficients with respect to the $\eta_k$ can be used to obtain the gradients of the $\mu(x_i)$ with respect to the $\eta_k$. The $\mu(x_i)$ have an implicit dependence on the $\bar{a}$, so the gradients of $\bar{a}$ have the form

$$\nabla_{\bar{\eta}} \mu(x_i) = \nabla_{\bar{a}} \mu(x_i) \cdot \nabla_{\bar{\eta}} \bar{a} \qquad (17)$$

The gradients of $\overline{\overline{K}}$ with respect to the $\bar{\eta}$ then have the form

$$\nabla_{\bar{\eta}} \overline{\overline{K}} = \nabla_{\bar{\mu}} \overline{\overline{K}} \cdot \nabla_{\bar{\eta}} \bar{\mu}$$

These can then be used to obtain the gradients of the objective function

$$\begin{aligned} \nabla_{\bar{\eta}} \chi \;=\; & -2 \left( \overline{\overline{K}}^{-1} g\bar{\rho} - \bar{u}_y \right) \\ & \cdot \cdot \overline{\overline{K}}^{-1} \nabla_{\bar{\eta}} \overline{\overline{K}} \cdot \overline{\overline{K}}^{-1} \cdot g\bar{\rho} \end{aligned} \qquad (18)$$

Again, the sparsity of $\nabla_{\bar{\mu}}$ can be used to speed up the calculation of the gradients.

The spline-based fits were tested on the parabolic velocity profile described above. Fits to the parabolic velocity profile using 4 and 16 knots were performed. A comparison of the profile obtained using the fitted value of $\mu$ with the original profile calculated using equation (11) is shown in figure 4 for a 4-knot fit. As can be seen from the figure, there is no discernible difference between the original and fitted curves. The viscosity profile from the fit is shown in figure 5. The figure shows a distinct parabolic variation, but the magnitude of the variation is negligible compared to the expected value of $\mu$. The viscosity profile obtained by using 16 knots is shown

in figure 6. This figure shows a more complicated variation than for the 4-knot fit, but again, the variations are minuscule compared to the expected value of $\mu$.

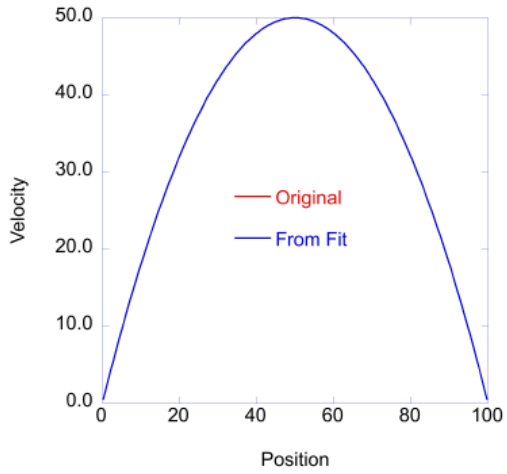


Figure 4. Parabolic velocity profile from equation (11) (red) and profile generated from least squares fit using cubic splines (blue) using 4 knots.

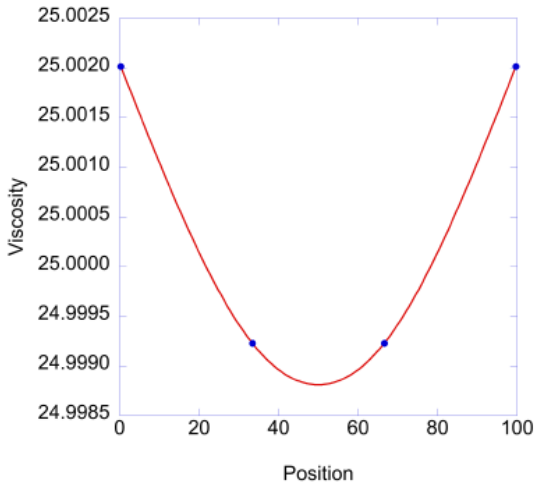


Figure 5. Viscosity profile from least squares fit to equation (11) using 4 knots. The interpolated values of $\mu(x)$ using the cubic splines are shown in red, the knot locations are shown as blue dots.

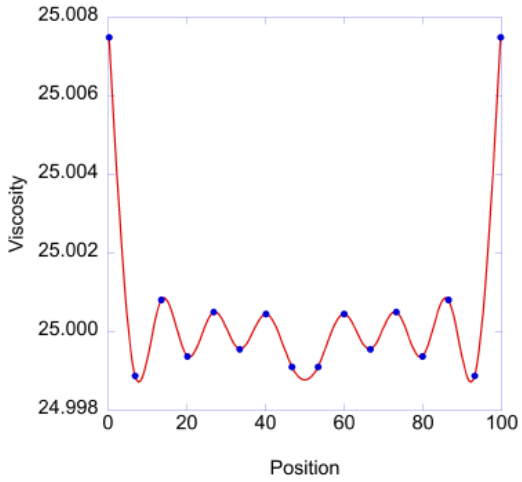


Figure 6. Viscosity profile from least squares fit to equation (11) using 16 knots. The interpolated values of $\mu(x)$ using the cubic splines are shown in red, the knot locations are shown as blue dots.

# 3.0 Results

To evaluate the effectiveness of the spline approach for real systems, classical molecular dynamics simulations of Poiseuille flow in a nanochannel were performed. Two systems were investigated, pure water between two slabs of talc and a 1M solution of NaCl in a pore of quartz-(001). The potential parameters for water were those of the SPC/E model [19]. The potential parameters for quartz, talc and the electrolyte ions were those of the CLAYFF model [20]. Molecular dynamics simulations were performed using the LAMMPS simulation package [21]. All simulations were equilibrated for 500 ps in the NPT ensemble at 300 K and 1 bar, in the direction of the confinement to relax the pore volume, as well as in the NVT ensemble for 5 ns. A Nosé–Hoover [22] thermostat with a time constant of 1 ps is applied to the solid atoms only. A time step of 1 fs was used to integrate the equations of motion. The equations of motion for the rigid water molecules were integrated using the SHAKE algorithm [23]. In order to simulate a Poiseuille flow, an acceleration of $4.7\times 10^{-5}$ $((\text{kcal}\cdot\text{mol}^{-1}\ \text{Å}^{-1})/(\text{g}\cdot\text{mol}^{-1}))$ per atom is applied in the $x$ direction. This value was chosen in the range where the response of the system is linear [24]. The subsequent flow trajectories were generated at 300 K for 20 ns, and steady-state velocity profiles were averaged over the 20 ns.

The velocity profiles and a corresponding series of spline fits are shown in figures 7 and 8. The water profile contains 290 data points and the NaCl profile contains 620 data points. Both simulations resulted in roughly parabolic velocity profiles. For pure water, the region near the channel boundaries shows signs of velocity slip and the profile drops suddenly near the wall. For NaCl, there are signs of a stagnation region near the boundary. This is usually interpreted as being due to a layer of ions that are strongly adsorbed to the wall, thereby effectively narrowing the width of the nano channel. Conventional analysis by fitting a velocity profile such as the NaCl solution to a parabola typically results in regions near the boundary where the parabolic profile goes negative. The flow is set to zero in these regions and the distance between the point at which the parabola is zero and the fluid boundary with the wall is interpreted as a negative slip length. Fitting a parabola to the pure water profile results in a profile that has a finite positive velocity at the boundary. The parabolic profile can be extrapolated to the point at which it goes to zero and the distance between that point and the boundary is interpreted as a positive slip length.

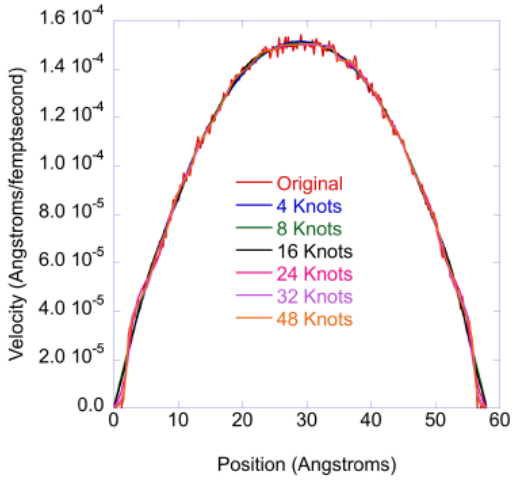


Figure 7. Molecular dynamics simulation of Poiseuille flow in a nano channel for pure water. Fits using 4, 8, 16, 24 32 and 48 knots are shown. The original simulation contains 290 data points.

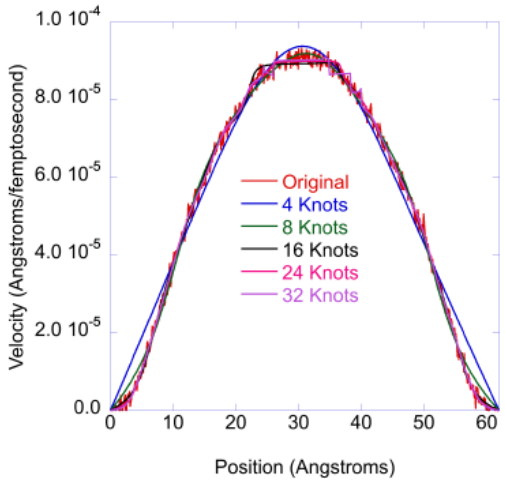


Figure 8. Molecular dynamics simulation of Poiseuille flow in a nano channel for 1M aqueous NaCl solution. Fits using 4, 8, 16, 24 32 and 48 knots are shown. The original simulation contains 620 data points.

For pure water, all spline fits appear to fall within the noise envelope of the simulations except for slight deviations near the boundaries of the channel. An expanded view of the velocity profile and the fits near the lefthand boundary is displayed in figure (9) and shows what appears to be some slippage at the boundary. The fits with a higher number of knots do an increasingly better job of capturing the flow profile near the wall but the same fits also start capturing the noise near the velocity maximum. This can be seen in figure (10), where the last three fits (24, 32 and 48 knots) show unphysical wiggles near the maximum. These wiggles stay within the noise envelop in the velocity profile and are unlikely to be reproducible across multiple runs. For the highest number of knots, the ratio of data points to knots is relatively low (290/48 ~ 6) but still high enough that 1) multiple data points are determining the value at the knot and 2) the spacing of data points is much smaller than the spacing of knots.

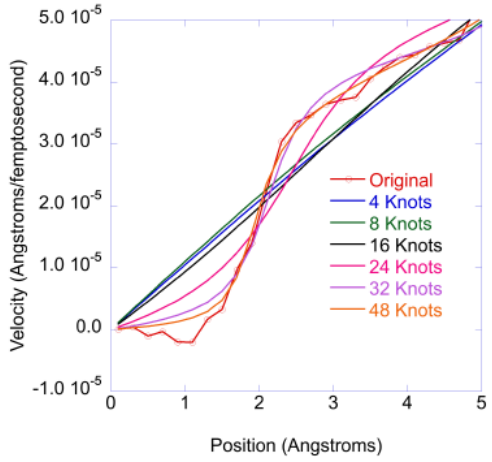


Figure 9. Expanded view of the profile shown in figure (7) near the boundary at $x = 0$.

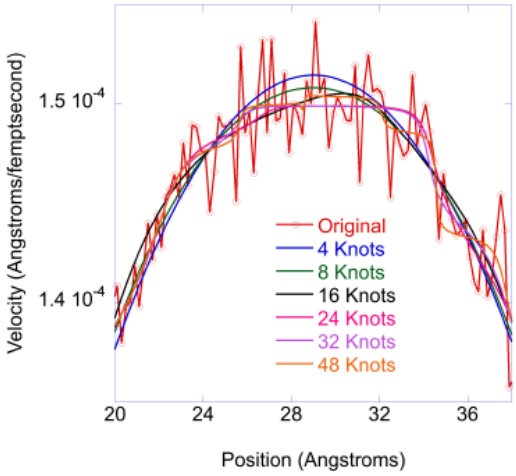


Figure 10. Expanded view of the profile shown in figure (7) near the maximum fluid velocity.

For the 1M NaCl solution, the fits using 4 and 8 knots are not doing a good job of capturing the flow profile near the channel walls. The 4-knot simulation also lies outside the noise envelope of the simulation in several other parts of the profile. At 16 knots, the fits fall inside the noise envelope and there is no noticeable improvement in the profile as the number of knots continues to increase. A closer look at the region near the velocity maximum in figure (11) shows quite odd behavior as the number of knots increases. Not only do wiggles appear in the fitted profile, but the velocity curve actually appears to be discontinuous. Whether this is a result of limited resolution in the $x$ increments or a result of instability in the linear solution of equation (9) was not determined.

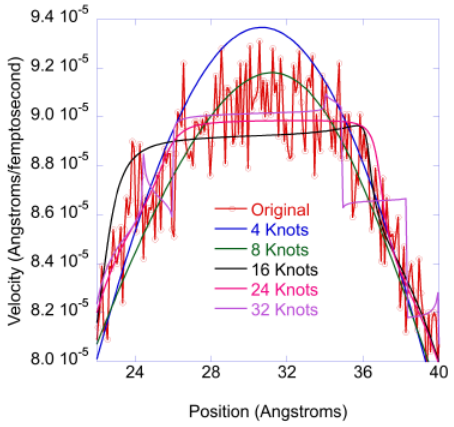


Figure 11. Expanded view of the profile shown in figure (8) near the maximum fluid velocity.

The corresponding viscosity profiles are shown in figures (12) and (13). The fits with larger numbers of knots all show substantial variations in the center of the channel as well as oscillations in other portions. The center of the channel is a region of low shear and the solution is likely insensitive to the value of the viscosity in this region, resulting in unrealistic values. Similar results have been obtained by other researchers using other approaches [18].

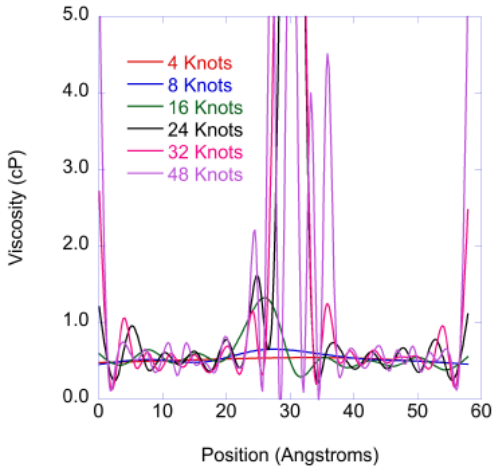


Figure 12. Viscosity profile for pure water in a nano channel. Fits using 4, 8, 16, 24, 32 and 48 knots are shown.

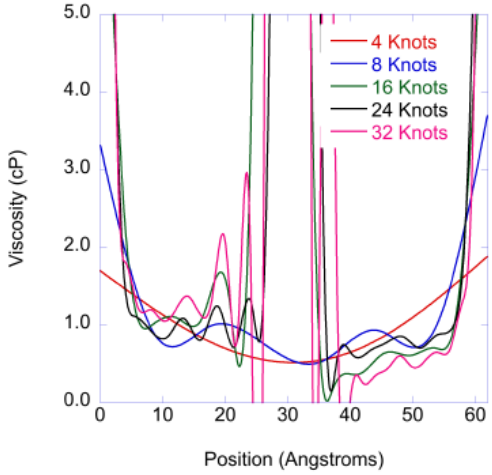


Figure 13. Viscosity profile for 1M aqueous NaCl solution in a nano channel. Fits using 4, 8, 16, 24 and 32 knots are shown.

For pure water, the fitted profile matches the behavior of the simulated velocity profile quite nicely. Apart from the instability at the center and some variation at the channel edges, the viscosity profile is fairly flat and centered at a value of about 0.5 cP. This is slightly lower than value reported by Předota et al. [18] which were closer to 0.8 cP, but those simulations used a different surface for the nano-channel as well as a different thermostat, so some differences can be expected. The value of 0.5 cP is closer to the values calculated by Simonnin et al. for SPC/E water in different clay nanopores, which ranged from 0.6 to 0.7 cP and also the values of 0.64-0.68 cP calculated by Tazi et al. [25] for bulk SPC/E water.

At the edges of the channel, there is a sharp rise in the value of the viscosity, although the actual magnitude of the rise is difficult to determine and varies considerably with the number of knots. Just before this rise, there is a dip in the viscosity that is consistent across all profiles calculated using a larger number of knots, starting at 16 knots. This low viscosity region corresponds roughly to the slip region seen in the viscosity profile. The increase in viscosity after the dip as one moves

towards the center of the channel also appears in all the higher knot fits but does not correspond to any distinctive feature in the velocity profile.

Compared to pure water, the NaCl solution shows a much broader region near the boundary where the viscosity is rapidly increasing. This matches the velocity profile, which also shows a wider region near the edges where flow is noticeably suppressed compared with the traditional parabolic profile. For the NaCl solution away from the boundary, the average viscosity appears to be higher than for pure water, somewhere in the range 0.8-1.0 cP. The profiles are more asymmetric than those for pure water, with curves to the left of center showing a higher viscosity than the curves to the right. We believe this is an indication of the uncertainty in the fits due to noise and finite sampling, since the simulated system itself should be symmetric about the center of the channel. Unlike the profile for water, there are no obvious features beyond the high viscosity regions at the boundaries. Although the boundary material for the simulations with and without salt is different, the increase in viscosity with dissolved salt matches behavior seen by Simonnin et al. [24] where adding 1M NaCl solutions increased the viscosity on the order of 0.15-0.2 cP over pure water.

Although the results of fits using different numbers of knots are approximately consistent, there is still wide variation in the viscosity profiles as the number of knots increases. This raises the question of whether or not there is a consistent way of choosing an optimal number of knots to get a profile that represents the best way of modeling the data. Given that the fits are unstable in the center of the channel, it would be desirable to use a minimum number of knots, since this increases the influence of regions outside the center in constraining the solution and suppressing large fluctuations.

One approach is to look at the behavior of the objective function when the fitted curve falls inside the noise envelope of the simulation results. When the curve is outside the noise envelope, there are systematic deviations between the fit and simulation. As these deviations get smaller with increasing numbers of knots, the value of the objective function will also improve significantly. However, once the fitted curve lies entirely within the noise envelope, the improvement with increasing knots will slow down, since the different curves are all relatively smooth and there are no regions where the fit and the data systematically diverge from each other. Finally, if the number of knots is increased to the point where they approach the number of data points, the fits will begin quantitatively modeling the noise and the objective function will start rapidly decreasing again.

With this in mind, it is instructive to look at plots of the objective function as a function of the number of knots, shown in figure 14. The absolute values of the objective functions are not significant, since the number of data points are different, but the two functions show qualitatively different behaviors. The lowest order fit to the pure water simulation was already almost completely contained inside the noise envelope of the simulation and the corresponding objective function shows relatively little variation as the number of knots increases. Figure (9) shows that the regions near the channel boundaries are accurately modeled for the 32 and 48 knot fits and partially captured by the 24-knot fit. Based on this, the 24 or 32 knot fit would be optimal. The objective function does not change much between 32 and 48 knots but still shows a relatively large decrease at 24 knots. However, all of the higher order fits (24, 32, and 48 knots) have significant wiggles near the maximum velocity.

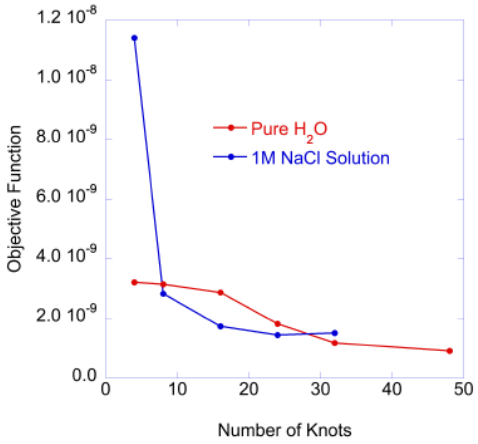


Figure 14. Objective functions for pure water and NaCl systems as a function of the number of knots.

The curve for the NaCl system shows a distinct break at 16 knots, which also corresponds to the point where the fitted profile moves inside the noise envelope. However, while the 16-knot fit captures the behavior near the boundary quite well, it also shows some unrealistic wiggles near the velocity maximum. The fitted profile does stay within the range of the simulated profile, even near the maximum and despite the wiggles.

Based on these observations, the 32-knot fit should be used for the pure water simulation and 16 knot fit used for the NaCl simulation. A comparison of the two profiles is shown in figure 15.

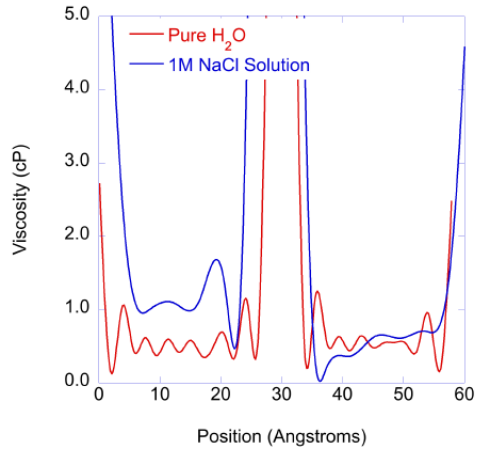


Figure 15. Viscosity profiles for pure water and 1M NaCl simulations. Pure water profile is from fit using 32 knots and 1M NaCl profile is from fit using 16 knots.

The channel widths for the two simulations are slightly different, hence the discrepancies in endpoints for the curves on the right-hand side. The function $\mu(x)$ is relatively symmetrical for water and shows a distinct dip near the channel edge that corresponds to the slippage seen in the velocity profile. Both edges show enhanced viscosity at the boundary as well as a smaller enhancement about 5 Å from the edges. The profile for the NaCl solution is much different. There is no low viscosity region near the boundary and the viscosity inside the channel is noticeably higher, although the asymmetry makes it difficult to say by how much. The viscosity profile also

exhibits sharp increases near the boundary that start about 6-7 Å from the edge. This is much wider than the corresponding region for the pure water simulation. The amount of increase also appears larger for the NaCl system but this may reflect noise in the simulation. The velocities in this region are small and may be overwhelmed by noise in the profile so the actual magnitude of the viscosity is likely to be highly uncertain. The width of the high viscosity region, on the other hand, appears to be consistent as the number of knots increases and figure (13) shows little variation in the width after 16 knots.

# 4.0 Conclusions

This paper describes a spline-based fitting method for obtaining viscosity profiles from simulations of Poiseuille flow in a nanochannel. The viscosity profiles are represented by a set of splines and the parameters in the spline functions are determined by a combination of continuity conditions on the splines themselves and a fit to the simulated velocity profile from the NEMD simulations. The use of splines, instead of just fitting a viscosity at every calculated value from the simulations, appears to lead to a more stable fit by reducing the number of fit parameters relative to the number of the measurements. For the simulations reported here, the worst-case scenario still resulted in at least 6 measurements per fitted parameter.

The spline fits were used to fit a test case, based on a classical parabolic flow profile, as well as realistic simulations of water and a 1M NaCl solution in a nanochannel. The test case was able to recover the analytic result for the viscosity to very high accuracy. For pure water and a 1M solution of NaCl, the results are in semi-quantitative agreement with other simulations, but differences in the surfaces of the slit pore and some simulation details rule out a quantitative comparison. A direct comparison of results obtained using the spline fitting approach described here and the methods described in Todd, Evans and Davis [11] using the same models and simulation methodology is currently in progress.

Solution and surface chemistry are expected to heavily influence molecular structures of confined liquids [26]. The apparent stickiness of the 1M NaCl solution near the channel boundaries and the slip observed near the walls for the pure water talc simulation suggests that viscosity is dependent on details of solution and surface chemistry. Effects such as charge states of the solid/liquid interfaces and ion specificity, which is critical to understand molecular scale flows in nanochannels, were demonstrated by a seminal study on dissipative responses by Granick [27]. Furthermore, additional features, such as the viscoelastic nature of confined aqueous liquids, probed by atomic force microscopy [26, 28, 29], may be important at these scales. The spline-based fitting scheme described here can potentially be extended to include viscoelastic shear stress coupling as well as other potentially relevant stress models similar to those used for polymeric liquids.

# 5.0 References

[1] M. P. Allen and D. J. Tildesley. Computer Simulation of Liquids. Oxford Clarendon Press, 1987.

[2] Melville S. Green. Markoff random processes and the statistical mechanics of time-dependent phenomena. II. Irreversible processes in fluids. The Journal of Chemical Physics, 22(3):398–413, 03 1954.

[3] Ryogo Kubo. Statistical-mechanical theory of irreversible processes. I. General theory and simple applications to magnetic and conduction problems. Journal of the Physical Society of Japan, 12(6):570–586, 1957.

[4] A W Lees and S F Edwards. The computer study of transport processes under extreme conditions. Journal of Physics C: Solid State Physics, 5(15):1921, Aug 1972.

[5] I.R. McDonald Eveline M. Gosling and K. Singer. On the calculation by molecular dynamics of the shear viscosity of a simple fluid. Molecular Physics, 26(6):1475–1484, 1973.

[6] Denis J. Evans and O.P. Morriss. Non-Newtonian molecular dynamics. Computer Physics Reports, 1(6):297–343, 1984.

[7] Christopher J. Mundy, Sundaram Balasubramanian, Ken Bagchi, Mark E. Tuckerman, Glenn J. Martyna, and Michael L. Klein. Nonequilibrium Molecular Dynamics, pages 291–397. John Wiley & Sons, Ltd, 2000.

[8] J. A. Morrone and B. J. Berne. Interplay between hydrodynamics and the free energy surface in the assembly of nanoscale hydrophobes. J. Phys. Chem. B, 116:378–389, Dec 2012.

[9] L. Cheng, P. Fenter, K. L. Nagy, M. L. Schlegel, and N. C. Sturchio. Molecular scale density oscillations in water adjacent to a mica surface. Phys. Rev. Lett., 87:156103, Sep 2001.

[10] T. D. Li and E. Riedo. Structured and viscous water in subnanometer gaps. Phys. Rev. B, 75:115415, March 2007.

[11] B. D. Todd, Denis J. Evans, and Peter J. Daivis. Pressure tensor for inhomogeneous fluids. Phys. Rev. E, 52:1627–1638, Aug 1995.

[12] Karl P. Travis, B. D. Todd, and Denis J. Evans. Departure from Navier-Stokes hydrodynamics in confined liquids. Phys. Rev. E, 55:4288–4295, Apr 1997.

[13] Joel Koplik, Jayanth R. Banavar, and Jorge F. Willemsen. Molecular dynamics of Poiseuille flow and moving contact lines. Phys. Rev. Lett., 60:1282–1285, Mar 1988.

[14] Alexandru Botan, Benjamin Rotenberg, Virginie Marry, Pierre Turq, and Benoît Noetinger. Hydrodynamics in clay nanopores. The Journal of Physical Chemistry C, 115(32):16109–16115, 2011.

[15] L. D. Landau and E. M. Lifschitz. Fluid Mechanics. Pergamon Press, 1982.

[16] Satish Balay, Shrirang Abhyankar, Mark F. Adams, Steven Benson, Jed Brown, Peter Brune, Kris Buschelman, Emil Constantinescu, Lisandro Dalcin, Alp Dener, Victor Eijkhout, Jacob Faibussowitsch, William D. Gropp, V´aclav Hapla, Tobin Isaac, Pierre Jolivet, Dmitry Karpeev, Dinesh Kaushik, Matthew G. Knepley, Fande Kong, Scott Kruger, Dave A. May, Lois Curfman McInnes, Richard Tran Mills, Lawrence Mitchell, Todd Munson, Jose E. Roman, Karl Rupp, Patrick Sanan, Jason Sarich, Barry F. Smith, Hansol Suh, Stefano Zampini, Hong Zhang, Hong Zhang, and Junchao Zhang. PETSc/TAO users manual. Technical Report ANL-21/39 – Revision 3.22, Argonne National Laboratory, 2024.

[17] C. de Boor. A Practical Guide to Splines. Springer-Verlag, 2001.

[18] M. Predota, P. T. Cummings, and D. J. Wesolowski. Electric double layer at the rutile (110) surface. 3. Inhomogeneous viscosity and diffusivity measurement by computer simulations. The Journal of Physical Chemistry C, 111(7):3071–3079, 2007.

[19] H. J. C. Berendsen, J. R. Grigera, and T. P. Straatsma. The missing term in effective pair potentials. The Journal of Physical Chemistry, 91(24):6269–6271, November 1987. Publisher: American Chemical Society.

[20] Randall T. Cygan, Jian-Jie Liang, and Andrey G. Kalinichev. Molecular Models of Hydroxide, Oxyhydroxide, and Clay Phases and the Development of a General Force Field. The Journal of Physical Chemistry B, 108(4):1255–1266, January 2004. Publisher: American Chemical Society.

[21] A. P. Thompson, H. M. Aktulga, R. Berger, D. S. Bolintineanu, W. M. Brown, P. S. Crozier, P. J. in 't Veld, A. Kohlmeyer, S. G. Moore, T. D. Nguyen, R. Shan, M. J. Stevens, J. Tranchida, C. Trott, and S. J. Plimpton. LAMMPS - a flexible simulation tool for particle-based materials modeling at the atomic, meso, and continuum scales. Comp. Phys. Comm., 271:108171, 2022.

[22] Glenn J Martyna, Michael L Klein, and Mark Tuckerman. Nos´e–Hoover chains: The canonical ensemble via continuous dynamics. The Journal of chemical physics, 97(4):2635–2643, 1992.

[23] Jean-Paul Ryckaert, Giovanni Ciccotti, and Herman J. C Berendsen. Numerical integration of the cartesian equations of motion of a system with constraints: molecular dynamics of n-alkanes. Journal of Computational Physics, 23(3):327–341, March 1977.

[24] Pauline Simonnin, Virginie Marry, Benoit Noetinger, Carlos Nieto-Draghi, and Benjamin Rotenberg. Mineral- and Ion-Specific Effects at Clay–Water Interfaces: Structure, Diffusion, and Hydrodynamics. The Journal of Physical Chemistry C, 122(32):18484–18492, August 2018. Publisher: American Chemical Society.

[25] Sami Tazi, Alexandru Bot ̧an, Mathieu Salanne, Virginie Marry, Pierre Turq, and Benjamin Rotenberg. Diffusion coefficient and shear viscosity of rigid water models. Journal of Physics: Condensed Matter, 24(28):284117, jun 2012.

[26] E. Nakouzi, A. G. Stack, S. Kerisit, B. A. Legg, C. J. Mundy, G. K. Schenter, J. Chun, and J. J. De Yoreo. Moving beyond the solvent-tip approximation to determine site-specific variations of interfacial water structure through 3d force microscopy. J. Phys. Chem. C, 125:1282–1291, Dec 2021.

[27] S. Granick. Motions and relaxations of confined liquids. Science, 253:1374–1379, Sep 1991.

[28] T. D. Li and E. Riedo. Nonlinear viscoelastic dynamics of nanoconfined wetting liquids. Phys. Rev. Lett., 100:106102, March 2008.

[29] T. D. Li, H. C. Chiu, D. Ortiz-Young, and E. Riedo. Nanorheology by atomic force microscopy. Rev. Sci. Instrum., 85:123707, Dec 2014.

# Pacific Northwest National Laboratory

902 Battelle Boulevard
P.O. Box 999
Richland, WA 99354

1-888-375-PNNL (7665)

***www.pnnl.gov***